Journal of Computational Physics 349 (2017) 441–452

Contents lists available at ScienceDirect

Journal of Computational Physics

www.elsevier.com/locate/jcp

Canonical symplectic structure and structure-preserving geometric algorithms for Schrödinger–Maxwell systems

Qiang Chen [a,b,*], Hong Qin [a,c,**], Jian Liu [a], Jianyuan Xiao [a], Ruili Zhang [a], Yang He [d], Yulei Wang [a]

[a] School of Nuclear Science and Technology and Department of Modern Physics, University of Science and Technology of China, Hefei, Anhui 230026, China
[b] Luoyang Electronic Equipment Testing Center, Luoyang 471000, China
[c] Plasma Physics Laboratory, Princeton University, Princeton, NJ 08543, USA
[d] School of Mathematics and Physics, University of Science and Technology Beijing, Beijing 100083, China

ARTICLE INFO

Article history:
Received 7 February 2017
Received in revised form 29 June 2017
Accepted 16 August 2017
Available online 24 August 2017

Keywords:
Schrödinger–Maxwell equations
Symplectic structure
Discrete Poisson bracket
Geometric algorithms
First-principle simulation

ABSTRACT

An infinite dimensional canonical symplectic structure and structure-preserving geometric algorithms are developed for the photon–matter interactions described by the Schrödinger–Maxwell equations. The algorithms preserve the symplectic structure of the system and the unitary nature of the wavefunctions, and bound the energy error of the simulation for all time-steps. This new numerical capability enables us to carry out first-principle based simulation study of important photon–matter interactions, such as the high harmonic generation and stabilization of ionization, with long-term accuracy and fidelity.

1. Introduction

Started with the photoelectric effect, photon–matter interaction has been studied over 100 years. With the establishment of the special relativity and quantum theory, scientists can make many accurate calculations to describe how photons are absorbed and emitted and how electrons are ionized and captured. Most of the work in early years were based on perturbative techniques, as the light source was so weak that only single photon effect was important. The accuracy maintained until the invention of chirped pulse amplification (CPA) for lasers in 1980s. Since then, the laser power density have increased 8 orders of magnitude, approaching 10^{22} W·cm^{-2}, which is stronger than the direct ionization threshold of $10^{16} \sim 10^{18}$ W·cm^{-2} [1,2]. Such a strong field brings many new physics, e.g., multiphoton ionization, above threshold ionization (ATI), high harmonic generation (HHG) and stabilization, which play a major role in modern high energy density physics, experimental astrophysics, attosecond physics, strong field electrodynamics and controlled fusion etc. [3–44]. There are several semi-classical non-perturbative methods to describe these phenomena, both analytical and numerical, and some experimental observations have been explained successfully [4,5,7,10,13,15–18,20,23,26,28,32,37]. Keldysh proposed the first

* Corresponding author at: School of Nuclear Science and Technology and Department of Modern Physics, University of Science and Technology of China, Hefei, Anhui 230026, China.
** Principal corresponding author at: School of Nuclear Science and Technology and Department of Modern Physics, University of Science and Technology of China, Hefei, Anhui 230026, China.
E-mail addresses: cq0405@ustc.edu.cn (Q. Chen), hongqin@ustc.edu.cn (H. Qin).

http://dx.doi.org/10.1016/j.jcp.2017.08.033
0021-9991/

non-perturbative theory describing the ionization process in a strong laser field [4]. It was then developed by Faisal and Reiss in the S matrix form known as KFR theory [5,7]. This theory was further developed into the rescattering methods [18, 26]. Simple man model is a classical model which gives an intuitive perspective to understand the ionization [10]. In semi-classical framework, the well known three-step model developed by Corkum gives a basic tool to study the strong field physics [15,45]. There are also some models based on quantum path-integral theory which output some detailed results about the transient paths [16,20]. Recently, relativistic corrections for strong field ionization was taken into consideration by Klaiber et al. [37]. Different from analytical models, directly solving the time-dependent Schrödinger equation (TDSE) is always a crucially important method for photon–matter interactions. By numerical simulations, Krause et al. obtained the cut-off law of HHG [13]. Nepstad et al. numerically studied the two-photon ionization of helium [28]. Birkeland et al. numerically studied the stabilization of helium in intense XUV laser fields [29]. Based on simulation results, much information about atom and molecular in strong field can be obtained [33,34]. Recently, multi-configuration methods were introduced into TDSE simulations to treat many-electron dynamics [46–48]. Because of the multi-scale nature of the process and the large number of degrees of freedom involved, most of the theoretical and numerical methods adopted various types of approximations for the Schrödinger equation, such as the strong field approximation [16], the finite energy levels approximation [49], the independent external field approximation [39] and the single-active electron approximation [13], which often have limited applicabilities [2,31]. To understand the intrinsic multi-scale, complex photon–matter interactions described by the Schrödinger–Maxwell (SM) equations, a comprehensive model needs to be developed by numerically solving the SM equations.

For the Maxwell equations, many numerical methods, such as the finite-difference time-domain method has been developed [50–52]. For the Schrödinger equation, unitary algorithm has been proposed [49,53–55]. Recently, a class of structure-preserving geometric algorithms have been developed for simulating classical particle-field interactions described by the Vlasov–Maxwell (VM) equations. Specifically, spatially discretized canonical and non-canonical Poisson brackets for the VM systems and associated symplectic time integration algorithms have been discovered and applied [56–65].

In this paper, we develop a new structure-preserving geometric algorithm for numerically solving the SM equations. For this purpose, the canonical symplectic structure of the SM equations is first established. Note that the canonical symplectic structure presented here is more transparent than the version given in Refs. [66,67], which involves complications due to a different choice of gauge. The structure-preserving geometric algorithm is obtained by discretizing the canonical Poisson bracket. The wavefunctions and gauge field are discretized point-wise on an Eulerian spatial grid, and the Hamiltonian functional is expressed as a function of the discretized fields. This procedure generates a finite-dimensional Hamiltonian system with a canonical symplectic structure. The degrees of freedom of the discrete system for a single electron atom discrete system is $4M$, where M is the number of grid points. For an ensemble of N single-active electron atoms, the discrete system has $(N+3)M$ degrees of freedom. A symplectic splitting algorithm is developed for semi-explicit time advance. The method inherits all the good numerical features of canonical symplectic algorithms, such as the long-term bound on energy–momentum error. We also design the algorithm such that it preserves unitary structure of the Schrödinger equation. These desirable features make the algorithm a powerful tool in the study of photon–matter interactions using the semi-classical model. We note the algorithm developed here for the SM equations is inspired by the recent advances in the structure-preserving geometric algorithms for classical particle-field interactions [56–65], especially the canonical particle-in-cell method [61].

2. Canonical symplectic structure of Schrödinger–Maxwell systems

In most strong field experiments, the atomic ensemble is weakly coupled, which means that electrons are localized around the nuclei and there is no direct coupling between different atoms. Electrons belong to different atoms are well resolved. In a single-active electron atomic ensemble, every electron can be labeled by a local atom potential. The wavefunction is a direct product of the resolved single electron wavefunctions. As the basic semi-classical model for photon–matter interactions between atomic ensemble and photons, the SM equations are

$$i\frac{\partial}{\partial t}\psi_i = \hat{H}_i\psi_i, \tag{1}$$

$$\partial_\mu F^{\mu\nu} = \sum_i \frac{4\pi}{c} J_i^\nu, \tag{2}$$

where $\hat{H}_i = \frac{(\boldsymbol{P}-\boldsymbol{A})^2}{2} + V_i$ is the Hamiltonian operator, $\boldsymbol{P} = -i\nabla$ is the canonical momentum, V_i is local atomic potential of the i-th atom, $F^{\mu\nu} = c(\partial^\mu A^\nu - \partial^\nu A^\mu)$ is the electromagnetic tensor, and c is the light speed in atomic units. The subscript i is electron label. The atomic potential can assume, for example, the form of $V_i(\boldsymbol{x}) = -\frac{Z}{|\boldsymbol{x}-\boldsymbol{x}_i|}$ with Z being atomic number and $\boldsymbol{x}_i$ the position of the atom. With metric signature $(+,-,-,-)$, in Eq. (2), $J_i^\mu = i\left[\psi_i^* D^\mu\psi_i - \psi_i(D^\mu\psi_i)^*\right]$ is the conserved Noether current, and $D_\mu = \partial_\mu + iA_\mu$ is the gauge-covariant derivative. In the nonrelativistic limit, the density J_i^0 reduces to $\psi_i^*\psi_i$, while the current density J_i^k reduces to $\frac{i}{2}\left[\psi_i^* D^k\psi_i - \psi_i(D^k\psi_i)^*\right]$, which closes the SM system. The temporal gauge $\phi = 0$ has been adopted explicitly.

The complex wavefunctions and Hamiltonian operators can be decomposed into real and imaginary parts,

$$\psi_i = \frac{1}{\sqrt{2}}\left(\psi_{iR} + i\psi_{iI}\right), \tag{3}$$

$$\hat{H}_i = \hat{H}_{iR} + i\hat{H}_{iI}, \tag{4}$$

$$\hat{H}_{iR} = \frac{1}{2}\left(-\nabla^2 + \boldsymbol{A}^2\right) + V_i, \quad \hat{H}_{iI} = \frac{1}{2}\nabla\cdot\boldsymbol{A} + \boldsymbol{A}\cdot\nabla. \tag{5}$$

In terms of the real and imaginary components, the Schrödinger equation is

$$\frac{\partial}{\partial t}\begin{pmatrix}\psi_{iR}\\ \psi_{iI}\end{pmatrix} = \begin{pmatrix}\hat{H}_{iI} & \hat{H}_{iR}\\ -\hat{H}_{iR} & \hat{H}_{iI}\end{pmatrix}\begin{pmatrix}\psi_{iR}\\ \psi_{iI}\end{pmatrix}. \tag{6}$$

The SM system admits an infinite dimensional canonical symplectic structure with following Poisson structure and Hamiltonian functional,

$$\{F, G\} = \int\left[\sum_i\left(\frac{\delta F}{\delta\psi_{iR}}\frac{\delta G}{\delta\psi_{iI}} - \frac{\delta G}{\delta\psi_{iR}}\frac{\delta F}{\delta\psi_{iI}}\right) + \frac{\delta F}{\delta\boldsymbol{A}}\frac{\delta G}{\delta\boldsymbol{Y}} - \frac{\delta G}{\delta\boldsymbol{A}}\frac{\delta F}{\delta\boldsymbol{Y}}\right]\mathrm{d}^3x, \tag{7}$$

$$\begin{aligned} H\left(\psi_{iR}, \psi_{iI}, \boldsymbol{A}, \boldsymbol{Y}\right) = \frac{1}{2}\int\Bigg[\sum_i\Big(&\psi_{iR}\hat{H}_{iR}\psi_{iR} + \psi_{iI}\hat{H}_{iR}\psi_{iI}\\ &- \psi_{iR}\hat{H}_{iI}\psi_{iI} + \psi_{iI}\hat{H}_{iI}\psi_{iR}\Big) + 4\pi\boldsymbol{Y}^2 + \frac{1}{4\pi}\left(c\nabla\times\boldsymbol{A}\right)^2\Bigg]\mathrm{d}^3x. \end{aligned} \tag{8}$$

Here, $\boldsymbol{Y} = \dot{\boldsymbol{A}}/4\pi$ and F, G, and H are functionals of $(\psi_{iR}, \psi_{iI}, \boldsymbol{A}, \boldsymbol{Y})$. The expression $\delta F/\delta\psi_{iR}$ is the variational derivative of the functional F with respect to ψ_{iR}, and other terms, e.g., $\delta F/\delta\psi_{iI}$ and $\delta F/\delta\boldsymbol{A}$, have similar meanings. The Hamiltonian functional $H\left(\psi_{iR}, \psi_{iI}, \boldsymbol{A}, \boldsymbol{Y}\right)$ in Eq. (8) is equivalent to the following expression in terms of the complex wavefunctions,

$$H\left(\psi_i^*, \psi_i, \boldsymbol{A}, \boldsymbol{Y}\right) = H_{qm} + H_{em}, \tag{9}$$

$$H_{qm} = \int\sum_i \psi_i^*\hat{H}_i\psi_i\mathrm{d}^3x, \tag{10}$$

$$H_{em} = \frac{1}{2}\int\left[4\pi\boldsymbol{Y}^2 + \frac{1}{4\pi}\left(c\nabla\times\boldsymbol{A}\right)^2\right]\mathrm{d}^3x. \tag{11}$$

Apparently, H_{em} is the Hamiltonian for the electromagnetic field, and H_{qm} is the Hamiltonian for the wavefunctions. In this infinite dimensional Hamiltonian system, the canonical pairs are (ψ_{iR}, ψ_{iI}) and $(\boldsymbol{A}, \boldsymbol{Y})$ at each spatial location. Their canonical equations are

$$\dot{\psi_{iR}} = \{\psi_{iR}, H\} = \frac{1}{2}\nabla\cdot\boldsymbol{A}\psi_{iR} + \boldsymbol{A}\cdot\nabla\psi_{iR} + \frac{1}{2}\left(-\nabla^2 + \boldsymbol{A}^2\right)\psi_{iI} + V_i\psi_{iI}, \tag{12}$$

$$\dot{\boldsymbol{A}} = \{\boldsymbol{A}, H\} = 4\pi\boldsymbol{Y}, \tag{13}$$

$$\dot{\psi_{iI}} = \{\psi_{iI}, H\} = \frac{1}{2}\left(\nabla^2 - \boldsymbol{A}^2\right)\psi_{iR} - V_i\psi_{iR} + \frac{1}{2}\nabla\cdot\boldsymbol{A}\psi_{iI} + \boldsymbol{A}\cdot\nabla\psi_{iI}, \tag{14}$$

$$\dot{\boldsymbol{Y}} = \{\boldsymbol{Y}, H\} = \mathcal{J} - \frac{c^2}{4\pi}\nabla\times\nabla\times\boldsymbol{A}, \tag{15}$$

where $\mathcal{J} = \frac{1}{2}\sum_i[\psi_{iR}\nabla\psi_{iI} - \psi_{iI}\nabla\psi_{iR} - (\psi_{iR}^2 + \psi_{iI}^2)\boldsymbol{A}]$ is the current density. In deriving Eqs. (12)–(15), use is made of the following expression of the total variation of Hamiltonian,

$$\begin{aligned} \delta H = \frac{1}{2}\int\sum_i[&\left(-\nabla^2\psi_{iR} + \boldsymbol{A}^2\psi_{iR} + 2V_i\psi_{iR} - 2\boldsymbol{A}\cdot\nabla\psi_{iI} - \nabla\cdot\boldsymbol{A}\psi_{iI}\right)\delta\psi_{iR}\\ &+\left(-\nabla^2\psi_{iI} + \boldsymbol{A}^2\psi_{iI} + 2V_i\psi_{iI} + 2\boldsymbol{A}\cdot\nabla\psi_{iR} + \nabla\cdot\boldsymbol{A}\psi_{iR}\right)\delta\psi_{iI}\\ &+\left(\psi_{iR}^2\boldsymbol{A} + \psi_{iI}^2\boldsymbol{A} + \psi_{iI}\nabla\psi_{iR} - \psi_{iR}\nabla\psi_{iI}\right)\cdot\delta\boldsymbol{A}]\mathrm{d}^3x\\ &+\int[\frac{c^2}{4\pi}\nabla\times\nabla\times\boldsymbol{A}\cdot\delta\boldsymbol{A} + 4\pi\boldsymbol{Y}\cdot\delta\boldsymbol{Y}]\mathrm{d}^3x, \end{aligned} \tag{16}$$

where integration by parts have been applied with fixed fields on the boundary.

3. Structure-preserving geometric algorithms for Schrödinger–Maxwell systems

We now present the structure-preserving geometric algorithms for numerically solving Eqs. (12)–(15). We discretize the fields $(\psi_{iR}, \psi_{iI}, \boldsymbol{A}, \boldsymbol{Y})$ on an Eulerian spatial grid as

$$\boldsymbol{A}(\boldsymbol{x},t)=\sum_{J=1}^{M}\boldsymbol{A}_J(t)\,\theta\left(\boldsymbol{x}-\boldsymbol{x}_J\right),\quad \boldsymbol{Y}(\boldsymbol{x},t)=\sum_{J=1}^{M}\boldsymbol{Y}_J(t)\,\theta\left(\boldsymbol{x}-\boldsymbol{x}_J\right), \tag{17}$$

$$\psi_{iR}(\boldsymbol{x},t)=\sum_{J=1}^{M}\psi_{iRJ}(t)\,\theta\left(\boldsymbol{x}-\boldsymbol{x}_J\right),\quad \psi_{iI}(\boldsymbol{x},t)=\sum_{J=1}^{M}\psi_{iIJ}(t)\,\theta\left(\boldsymbol{x}-\boldsymbol{x}_J\right), \tag{18}$$

where the distribution function $\theta\left(\boldsymbol{x}-\boldsymbol{x}_J\right)$ is defined as

$$\theta\left(\boldsymbol{x}-\boldsymbol{x}_J\right)=\begin{cases}1, & |x-x_J|<\frac{\triangle x}{2},|y-y_J|<\frac{\triangle y}{2},|z-z_J|<\frac{\triangle z}{2}\\ 0, & elsewhere\end{cases}. \tag{19}$$

Then, the variational derivative with respect to $\boldsymbol{A}$ is

$$\frac{\delta F}{\delta \boldsymbol{A}}=\sum_{J=1}^{M}\frac{\delta \boldsymbol{A}_J}{\delta \boldsymbol{A}}\frac{\partial F}{\partial \boldsymbol{A}_J}=\sum_{J=1}^{M}\frac{1}{\triangle V}\theta\left(\boldsymbol{x}-\boldsymbol{x}_J\right)\frac{\partial F}{\partial \boldsymbol{A}_J}, \tag{20}$$

and the variational derivatives with respect to $\boldsymbol{Y}$, ψ_{iR} and ψ_{iI} have similar expressions. Here, $\triangle V=\triangle x\triangle y\triangle z$ is the volume of each cell. The canonical Poisson bracket is discretized as

$$\{F,G\}_d=\sum_{J=1}^{M}\left[\sum_i\left(\frac{\partial F}{\partial \psi_{iRJ}}\frac{\partial G}{\partial \psi_{iIJ}}-\frac{\partial G}{\partial \psi_{iRJ}}\frac{\partial F}{\partial \psi_{iIJ}}\right)+\frac{\partial F}{\partial \boldsymbol{A}_J}\frac{\partial G}{\partial \boldsymbol{Y}_J}-\frac{\partial G}{\partial \boldsymbol{A}_J}\frac{\partial F}{\partial \boldsymbol{Y}_J}\right]\frac{1}{\triangle V}. \tag{21}$$

The Hamiltonian functional is discretized as

$$H_d\left(\psi_{iRJ},\psi_{iIJ},\boldsymbol{A}_J,\boldsymbol{Y}_J\right)=H_{dem}+H_{dqm}, \tag{22}$$

$$H_{dem}=\frac{1}{2}\sum_{J=1}^{M}\left[4\pi\boldsymbol{Y}_J^2+\frac{1}{4\pi}\left(c\bigtriangledown_d\times\boldsymbol{A}\right)_J^2\right]\triangle V, \tag{23}$$

$$\begin{aligned}H_{dqm}=\frac{1}{2}\sum_{J=1}^{M}\sum_i\Bigg[&-\frac{1}{2}\psi_{iRJ}\left(\bigtriangledown_d^2\psi_{iR}\right)_J-\frac{1}{2}\psi_{iIJ}\left(\bigtriangledown_d^2\psi_{iI}\right)_J-\psi_{iRJ}\boldsymbol{A}_J\cdot\left(\bigtriangledown_d\psi_{iI}\right)_J\\&+\psi_{iIJ}\boldsymbol{A}_J\cdot\left(\bigtriangledown_d\psi_{iR}\right)_J+\left(\frac{1}{2}\boldsymbol{A}_J^2+V_{iJ}\right)\left(\psi_{iRJ}^2+\psi_{iIJ}^2\right)\Bigg]\triangle V,\end{aligned} \tag{24}$$

where $V_{iJ}=V_i\left(\boldsymbol{x}_J\right)$, and the discrete spatial operators are defined as

$$\left(\bigtriangledown_d\psi\right)_J=\begin{pmatrix}\frac{\psi_{i,j,k}-\psi_{i-1,j,k}}{\triangle x}\\ \frac{\psi_{i,j,k}-\psi_{i,j-1,k}}{\triangle y}\\ \frac{\psi_{i,j,k}-\psi_{i,j,k-1}}{\triangle z}\end{pmatrix}, \tag{25}$$

$$\left(\bigtriangledown_d\cdot\boldsymbol{A}\right)_J=\frac{Ax_{i,j,k}-Ax_{i-1,j,k}}{\triangle x}+\frac{Ay_{i,j,k}-Ay_{i,j-1,k}}{\triangle y}+\frac{Az_{i,j,k}-Az_{i,j,k-1}}{\triangle z}, \tag{26}$$

$$\left(\bigtriangledown_d\times\boldsymbol{A}\right)_J=\begin{pmatrix}\frac{Az_{i,j,k}-Az_{i,j-1,k}}{\triangle y}-\frac{Ay_{i,j,k}-Ay_{i,j,k-1}}{\triangle z}\\ \frac{Ax_{i,j,k}-Ax_{i,j,k-1}}{\triangle z}-\frac{Az_{i,j,k}-Az_{i-1,j,k}}{\triangle x}\\ \frac{Ay_{i,j,k}-Ay_{i-1,j,k}}{\triangle x}-\frac{Ax_{i,j,k}-Ax_{i,j-1,k}}{\triangle y}\end{pmatrix}, \tag{27}$$

$$\left(\bigtriangledown_d^2\psi\right)_J=\frac{\psi_{i,j,k}-2\psi_{i-1,j,k}+\psi_{i-2,j,k}}{\triangle x^2}+\frac{\psi_{i,j,k}-2\psi_{i,j-1,k}+\psi_{i,j-2,k}}{\triangle y^2}+\frac{\psi_{i,j,k}-2\psi_{i,j,k-1}+\psi_{i,j,k-2}}{\triangle z^2}. \tag{28}$$

Here, the subscript J denotes grid position (i,j,k). The discrete spatial operators defined here use first order backward difference schemes. High order spatial schemes can be developed as well.

The discrete canonical equations are

$$\begin{aligned}\dot{\psi_{iRJ}} &= \{\psi_{iRJ}, H_d\}_d \\ &= \frac{1}{2}\boldsymbol{A}_J\cdot(\nabla_d\psi_{iR})_J - \frac{1}{2}\sum_{K=1}^{M}\psi_{iRK}\boldsymbol{A}_K\cdot\frac{\partial}{\partial\psi_{iIJ}}(\nabla_d\psi_{iI})_K \\ &\quad - \frac{1}{4}\left(\nabla_d^2\psi_{iI}\right)_J - \frac{1}{4}\sum_{K=1}^{M}\psi_{iIK}\frac{\partial}{\partial\psi_{iIJ}}\left(\nabla_d^2\psi_{iI}\right)_K + \left(\frac{1}{2}\boldsymbol{A}_J^2 + V_{iJ}\right)\psi_{iIJ}, \end{aligned} \tag{29}$$

$$\dot{\boldsymbol{A}}_J = \{\boldsymbol{A}_J, H_d\}_d = 4\pi\boldsymbol{Y}_J, \tag{30}$$

$$\begin{aligned}\dot{\psi_{iIJ}} &= \{\psi_{iIJ}, H_d\}_d \\ &= \frac{1}{4}\left(\nabla_d^2\psi_{iR}\right)_J + \frac{1}{4}\sum_{K=1}^{M}\psi_{iRK}\frac{\partial}{\partial\psi_{iRJ}}\left(\nabla_d^2\psi_{iR}\right)_K - \left(\frac{1}{2}\boldsymbol{A}_J^2 + V_{iJ}\right)\psi_{iRJ} \\ &\quad + \frac{1}{2}\boldsymbol{A}_J\cdot(\nabla_d\psi_{iI})_J - \frac{1}{2}\sum_{K=1}^{M}\psi_{iIK}\boldsymbol{A}_K\cdot\frac{\partial}{\partial\psi_{iRJ}}(\nabla_d\psi_{iR})_K, \end{aligned} \tag{31}$$

$$\dot{\boldsymbol{Y}}_J = \{\boldsymbol{Y}_J, H_d\}_d = \mathcal{J}_J - \frac{c^2}{4\pi}\left(\nabla_d^T\times\nabla_d\times\boldsymbol{A}\right)_J, \tag{32}$$

where $\mathcal{J}_J = \frac{1}{2}\sum_i[\psi_{iRJ}(\nabla_d\psi_{iI})_J - \psi_{iIJ}(\nabla_d\psi_{iR})_J - \boldsymbol{A}_J\left(\psi_{iRJ}^2 + \psi_{iIJ}^2\right)]$ is the discrete current density. The last term in Eq. (32) is defined to be,

$$\left(\nabla_d^T\times\nabla_d\times\boldsymbol{A}\right)_J \equiv \frac{1}{2}\frac{\partial}{\partial\boldsymbol{A}_J}\left[\sum_{K=1}^{M}(\nabla_d\times\boldsymbol{A})_K^2\right], \tag{33}$$

which indicates that the right-hand side of Eq. (33) can be viewed as the discretized $\nabla\times\nabla\times\boldsymbol{A}$ for a well-chosen discrete curl operator $\nabla_d\times$.

We will use the following symplectic splitting algorithms to numerically solve this set of discrete canonical Hamiltonian equations. In Eq. (22), H_d is naturally split into two parts, each of which corresponds to a subsystem that will be solved independently. The solution maps of the subsystems will be combined in various ways to give desired algorithms for the full system. For the subsystem determined by H_{dqm}, the dynamic equations are

$$\begin{aligned}\dot{\psi_{iRJ}} &= \{\psi_{iRJ}, H_{dqm}\}_d \\ &= \frac{1}{2}\boldsymbol{A}_J\cdot(\nabla_d\psi_{iR})_J - \frac{1}{2}\sum_{K=1}^{M}\psi_{iRK}\boldsymbol{A}_K\cdot\frac{\partial}{\partial\psi_{iIJ}}(\nabla_d\psi_{iI})_K \\ &\quad - \frac{1}{4}\left(\nabla_d^2\psi_{iI}\right)_J - \frac{1}{4}\sum_{K=1}^{M}\psi_{iIK}\frac{\partial}{\partial\psi_{iIJ}}\left(\nabla_d^2\psi_{iI}\right)_K + \left(\frac{1}{2}\boldsymbol{A}_J^2 + V_{iJ}\right)\psi_{iIJ}, \end{aligned} \tag{34}$$

$$\begin{aligned}\dot{\psi_{iIJ}} &= \{\psi_{iIJ}, H_{dqm}\}_d \\ &= \frac{1}{4}\left(\nabla_d^2\psi_{iR}\right)_J + \frac{1}{4}\sum_{K=1}^{M}\psi_{iRK}\frac{\partial}{\partial\psi_{iRJ}}\left(\nabla_d^2\psi_{iR}\right)_K - \left(\frac{1}{2}\boldsymbol{A}_J^2 + V_{iJ}\right)\psi_{iRJ} \\ &\quad + \frac{1}{2}\boldsymbol{A}_J\cdot(\nabla_d\psi_{iI})_J - \frac{1}{2}\sum_{K=1}^{M}\psi_{iIK}\boldsymbol{A}_K\cdot\frac{\partial}{\partial\psi_{iRJ}}(\nabla_d\psi_{iR})_K, \end{aligned} \tag{35}$$

$$\dot{\boldsymbol{A}}_J = \{\boldsymbol{A}_J, H_{dqm}\}_d = 0, \tag{36}$$

$$\dot{\boldsymbol{Y}}_J = \{\boldsymbol{Y}_J, H_{dqm}\}_d = \mathcal{J}_J. \tag{37}$$

Equations (34) and (35) can be written as

$$\frac{d}{dt}\begin{pmatrix}\psi_{iR}\\ \psi_{iI}\end{pmatrix} = \Omega(\boldsymbol{A})\begin{pmatrix}\psi_{iR}\\ \psi_{iI}\end{pmatrix}, \tag{38}$$

where $\Omega(\boldsymbol{A})$ is an skew-symmetric matrix. It easy to show that $\Omega(\boldsymbol{A})$ is also an infinitesimal generator of the symplectic group. To preserve the unitary property of ψ_i, we adopt the symplectic mid-point method for this subsystem, and the one step map $M_{qm}:(\psi_i,\boldsymbol{A},\boldsymbol{Y})^n \longmapsto (\psi_i,\boldsymbol{A},\boldsymbol{Y})^{n+1}$ is given by

$$\begin{pmatrix}\psi_{iR}\\ \psi_{iI}\end{pmatrix}^{n+1}=\begin{pmatrix}\psi_{iR}\\ \psi_{iI}\end{pmatrix}^{n}+\frac{\Delta t}{2}\Omega(\boldsymbol{A}^n)\left[\begin{pmatrix}\psi_{iR}\\ \psi_{iI}\end{pmatrix}^{n}+\begin{pmatrix}\psi_{iR}\\ \psi_{iI}\end{pmatrix}^{n+1}\right], \tag{39}$$

$$\boldsymbol{A}^{n+1}=\boldsymbol{A}^n, \tag{40}$$

$$\boldsymbol{Y}^{n+1}=\boldsymbol{Y}^n+\Delta t\mathcal{J}\left(\frac{\psi_{iR}^n+\psi_{iR}^{n+1}}{2},\frac{\psi_{iI}^n+\psi_{iI}^{n+1}}{2}\right). \tag{41}$$

Equation (39) is a linear equation in terms of $(\psi_{iR}^{n+1},\psi_{iI}^{n+1})$. Its solution is

$$\begin{pmatrix}\psi_{iR}\\ \psi_{iI}\end{pmatrix}^{n+1}=Cay(\Omega(\boldsymbol{A}^n)\frac{\Delta t}{2})\begin{pmatrix}\psi_{iR}\\ \psi_{iI}\end{pmatrix}^{n}, \tag{42}$$

$$Cay(\Omega(\boldsymbol{A}^n)\frac{\Delta t}{2})=\left(1-\Omega(\boldsymbol{A}^n)\frac{\Delta t}{2}\right)^{-1}\left(1+\Omega(\boldsymbol{A}^n)\frac{\Delta t}{2}\right), \tag{43}$$

where $Cay(S)$ denotes the Cayley transformation of matrix S. It is well-known that $Cay(S)$ is a symplectic rotation matrix when S in the Lie algebra of the symplectic rotation group. Thus, the one-step map from $\psi_i^n=\psi_{iR}^n+i\psi_{iI}^n$ to $\psi_i^{n+1}=\psi_{iR}^{n+1}+i\psi_{iI}^{n+1}$ induced by M_{qm} for the subsystem H_{dqm} is unitary. Since $\Omega(\boldsymbol{A}^n\Delta t/2)$ is a sparse matrix, there exist efficient algorithms to solve Eq. (39) or to calculate $Cay(\Omega(\boldsymbol{A}^n)\Delta t/2)$. Once ψ_i^{n+1} is known, $\boldsymbol{Y}^{n+1}$ can be calculated explicitly. Thus, $M_{qm}:(\psi_i,\boldsymbol{A},\boldsymbol{Y})^n\longmapsto(\psi_i,\boldsymbol{A},\boldsymbol{Y})^{n+1}$ is a second-order symplectic method, which also preserves the unitariness of ψ_i.

For the subsystem H_{dem}, the dynamic equations are

$$\dot{\psi_{iRJ}}=\{\psi_{iRJ},H_{dem}\}_d=0, \tag{44}$$

$$\dot{\psi_{iIJ}}=\{\psi_{iIJ},H_{dem}\}_d=0, \tag{45}$$

$$\dot{\boldsymbol{A}_J}=\{\boldsymbol{A}_J,H_{dem}\}_d=4\pi\boldsymbol{Y}_J, \tag{46}$$

$$\dot{\boldsymbol{Y}_J}=\{\boldsymbol{Y}_J,H_{dem}\}_d=-\frac{c^2}{4\pi}\left(\nabla_d^T\times\nabla_d\times\boldsymbol{A}\right)_J. \tag{47}$$

Equations (46) and (47) are linear in terms of $\boldsymbol{A}$ and $\boldsymbol{Y}$, and can be written as

$$\frac{d}{dt}\begin{pmatrix}\boldsymbol{A}\\ \boldsymbol{Y}\end{pmatrix}=Q\begin{pmatrix}\boldsymbol{A}\\ \boldsymbol{Y}\end{pmatrix}, \tag{48}$$

where Q is a constant matrix. We also use the second order symplectic mid-point rule for this subsystem, and the one step map $M_{em}:(\psi_i,\boldsymbol{A},\boldsymbol{Y})^n\longmapsto(\psi_i,\boldsymbol{A},\boldsymbol{Y})^{n+1}$ is given explicitly by

$$\begin{pmatrix}\psi_{iR}\\ \psi_{iI}\end{pmatrix}^{n+1}=\begin{pmatrix}\psi_{iR}\\ \psi_{iI}\end{pmatrix}^{n}, \tag{49}$$

$$\begin{pmatrix}\boldsymbol{A}\\ \boldsymbol{Y}\end{pmatrix}^{n+1}=Cay\left(Q\frac{\Delta t}{2}\right)\begin{pmatrix}\boldsymbol{A}\\ \boldsymbol{Y}\end{pmatrix}^{n}. \tag{50}$$

Since the map does not change ψ_i, it is unitary.

Given the second-order symmetric symplectic one-step maps M_{em} and M_{qm} for the subsystems H_{dem} and H_{dqm}, respectively, various symplectic algorithms for the system can be constructed by composition. For example, a first-order algorithm for H_d is

$$M(\Delta t)=M_{em}(\Delta t)\circ M_{qm}(\Delta t). \tag{51}$$

A second-order symplectic symmetric method can be constructed by the following symmetric composition,

$$M^2(\Delta t)=M_{em}(\Delta t/2)\circ M_{qm}(\Delta t)\circ M_{em}(\Delta t/2). \tag{52}$$

From a $2l$-th order symplectic symmetric method $M^{2l}(\Delta t)$, a $2(l+1)$-th order symplectic symmetric method can be constructed as

$$M^{2(l+1)}(\Delta t)=M^{2l}(\alpha_l\Delta t)\circ M^{2l}(\beta_l\Delta t)\circ M^{2l}(\alpha_l\Delta t), \tag{53}$$

$$\text{with }\alpha_l=\left(2-2^{1/(2l+1)}\right)^{-1},\ \text{and }\beta_l=1-2\alpha_l. \tag{54}$$

Obviously, the composed algorithms for the full system is symplectic and unitary.

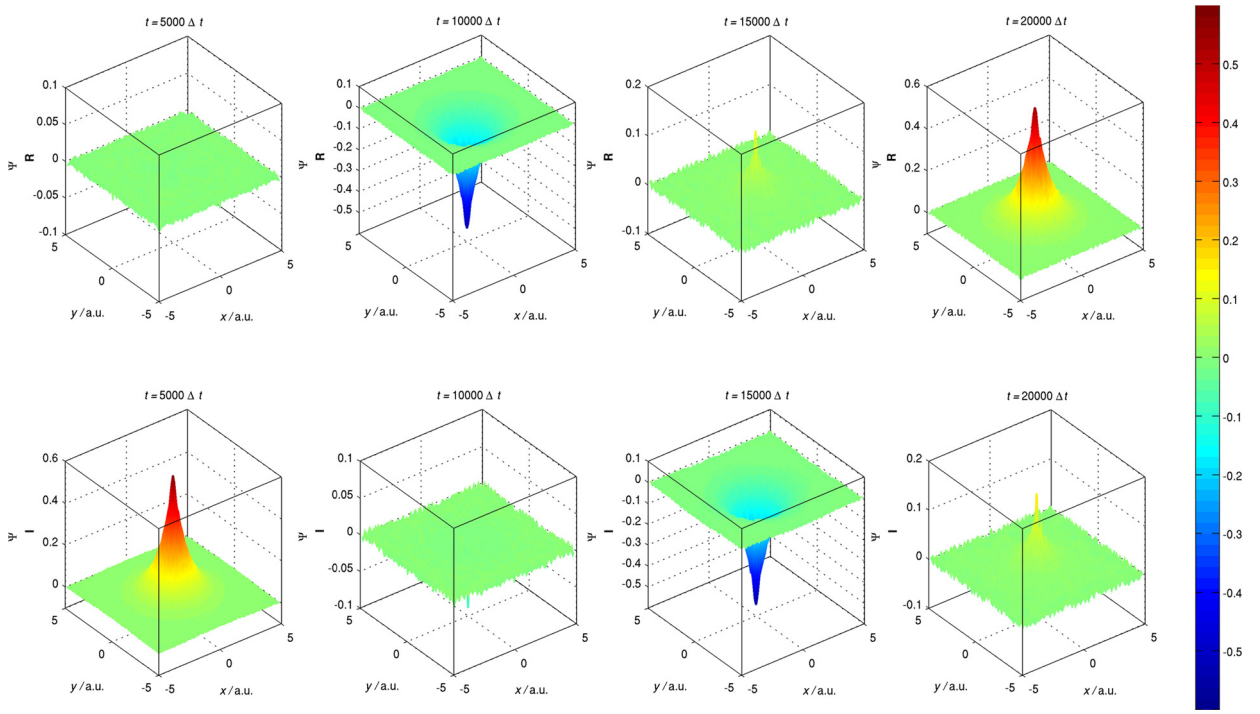

Fig. 1. Oscillation of the wavefunction for a hydrogen atom. The real and imaginary parts of wave function on the $z = 0$ plane which passes through the nuclear center. One oscillation cycle is shown.

4. Numerical examples

As numerical examples, two semi-classical problems have been solved using an implementation of the first-order structure-preserving geometric algorithm described above. Simulations are carried out on a Scientific Linux 6.3 OS with two 2.1 GHz Intel Core2 CPUs. The data structure is designed in coordinate sparse format and the BICGSTAB method (iteration accuracy 10^{-9}) is introduced to implement the Cayley transformation.

The first numerical example is the oscillation of a free hydrogen atom, which has been well studied both theoretically and experimentally [68,69]. The simulation domain is a $100 \times 100 \times 100$ uniform Cartesian grid, which represents a $[-5, 5] \times [-5, 5] \times [-5, 5]$ a.u.^{3} physical space. All boundaries are periodic. A hydrogen nucleus is fixed on the origin and the initial wave function is a direct discretization of the ground-state wavefunction $\psi = \frac{1}{\sqrt{\pi}} e^{-r}$. The time step is $\triangle t = 1.5\delta/\sqrt{3}c$ a.u., where $\delta = \triangle x = \triangle y = \triangle z = 0.1$ a.u. and $c \approx 137$ a.u. A total of 2×10^4 simulation steps covers a complete oscillation cycle of the ground state. Simulation results show the ground-state oscillation with very small numerical noise. Due to the finite-grid size effect and self-field effect, the initial wave function is not the exact numerical ground state of discrete hydrogen atom. It is only a good approximation, which couples weakly to other energy levels. The real and imaginary parts of the wavefunction on the $z = 0$ plane at four different times are plotted in Fig. 1. The numerical oscillation period is found to be 12.58 a.u., which agrees the analytical result 4π a.u. very well. The mode structures at the frequency $\nu = 1/4\pi$ a.u. are plotted in Fig. 2. As expected, the structure-preserving geometric algorithm has excellent long-term properties. The time-history of numerical errors are plotted in Fig. 3. After a long-term simulation, both total probability error and total Hamiltonian error are bounded by a small value.

In the second example, we simulate the continuous ionization of a hydrogen atom in an ultrashort intense pulse-train of electromagnetic field. Because the light-electron speed ratio is about 137, the coupling between a single ultrashort pulse and the atom is weak. But with the continuous excitation by the intense pulse-train, the atom can be ionized gradually. The computation domain and initial wavefunction are the same as the first example, and the time step is chosen to $\triangle t = 0.1\delta/\sqrt{3}c$ a.u. to capture the scattering process. To introduce the incident pulse-train, we set the initial gauge field to be $\boldsymbol{A}^0 = 100e^{-(z+2.5)^2/0.25}\boldsymbol{e}_x$ and $\boldsymbol{Y}^0 = 0$, representing two linearly-polarized modulated Gaussian waves which counter-propagate along the z-direction. The evolution of wave function is plotted in Figs. 4 and 5, which depicts the continuous ionization process by the ultrashort intense pulse-train. The ionization is indicated by the increasing plane-wave components of the wavefunction. Fig. 6 illustrates the evolution of scattered gauge field, which dependents strongly on the electron polarization current. To demonstrate the excellent long-term properties of the structure-preserving geometric algorithm, the time-history of numerical errors in this example are plotted in Fig. 7. After a long-term simulation, the numerical errors of conservation quantities are bounded by a small value.

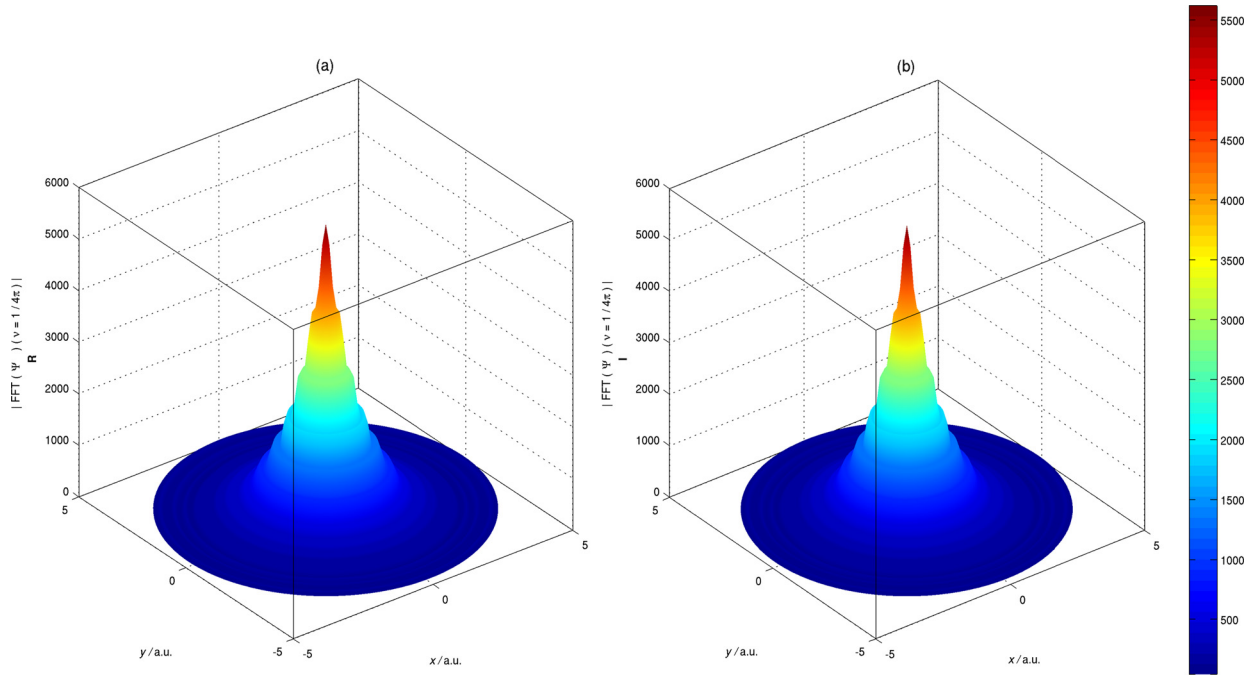

Fig. 2. Mode structure of the ground state. Real part (a) and imaginary part (b) on $z = 0$ plane are plotted for the frequency component at $\nu = 1/4\pi$ a.u.

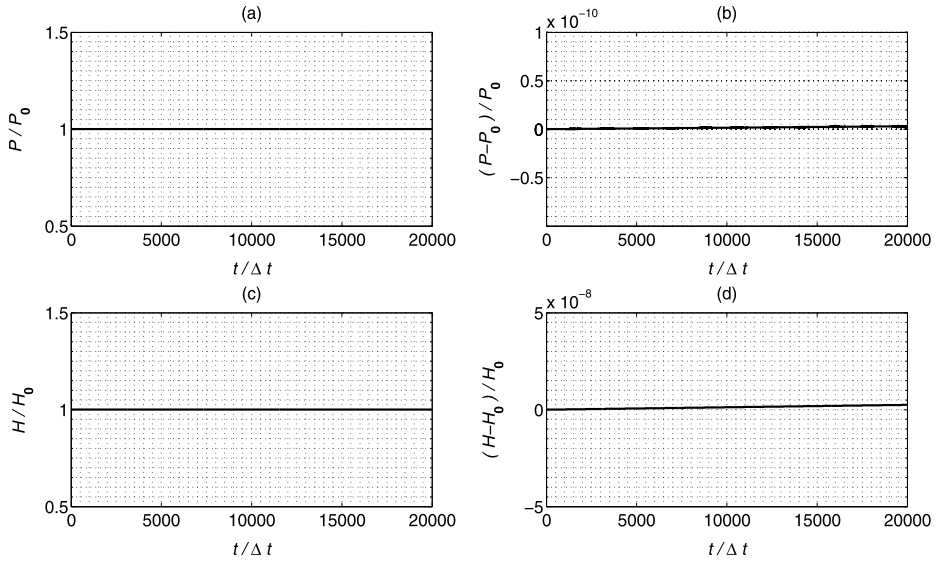

Fig. 3. Time-history of numerical errors. After a long-term simulation, both total probability error (a)–(b) and total Hamiltonian error (c)–(d) are bounded by a small value.

5. Conclusions

The structure-preserving geometric algorithms developed provide us with a first-principle based simulation capability for the SM system with long-term accuracy and fidelity. Two numerical examples validated the algorithm and demonstrated its applications. This approach is particularly valuable when the laser intensity reaches 10^{18} W·cm^{-2}, which invalidates many reduced or simplified theoretical and numerical models based on perturbative analysis. For example, structure-preserving geometric algorithms can be applied to achieve high fidelity simulations of the HHG physics and the stabilization effect of ionization. The HHG has been partially explained by the three-step semi-classical model and the Lewenstein model in the strong field approximation [13,15,16]. After ionization, acceleration and recapture in a strong field, the electron emits photons with a high order harmonic spectrum. The step and cutoff structures of the spectrum strongly depend on the beam intensity, photon energy and atomic potential. With the time dependent wave function, the spectrum $F(\omega) =$

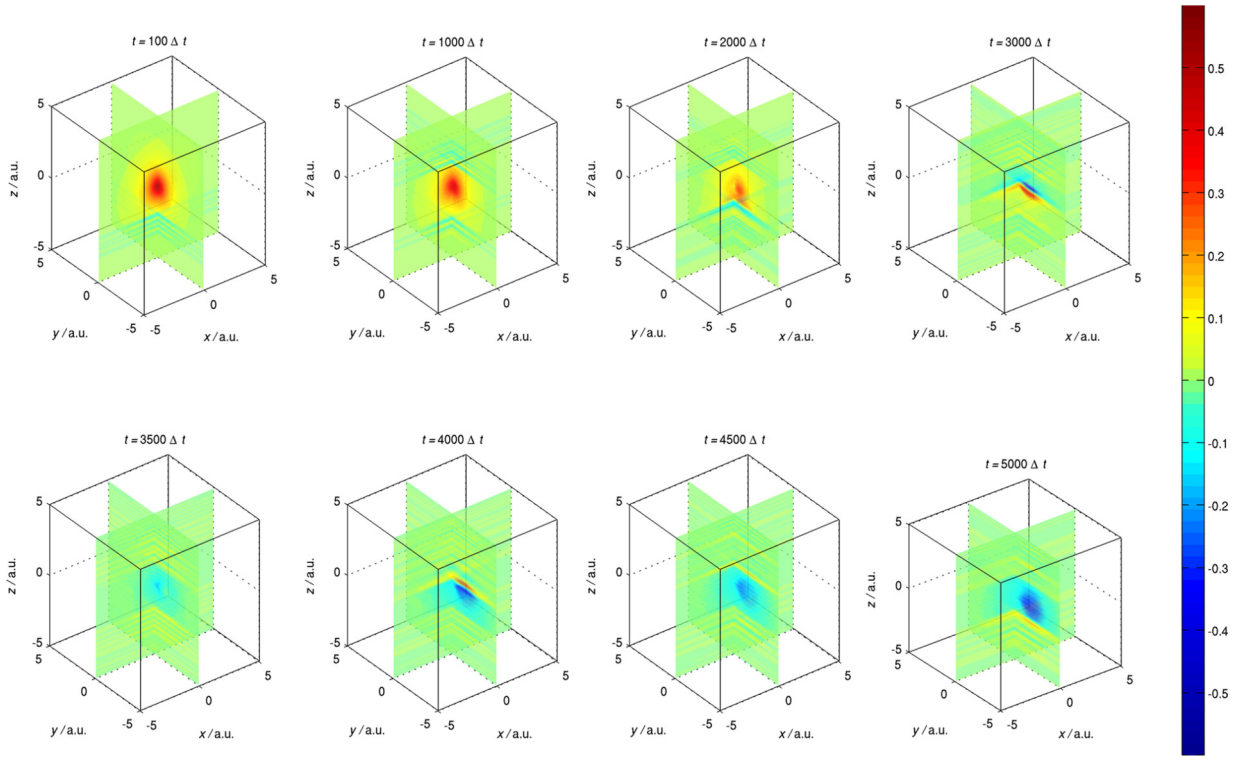

Fig. 4. Evolution of the wavefunction (real part). It shows that at early time, the wave function is localized and the atomic state is maintained. After a few pulses, the wave function is slightly modified by the gauge field and plane wave components along the z-direction can be found, which marks the beginning of ionization. With the accumulation of pulse-train, the wave function drifts along the $\boldsymbol{A} \times \boldsymbol{k}$ direction, and the atomic state is broken. The increasing plane-wave components due to ionization can be clearly identified. In this process, photon momentum is transferred to the electron gradually.

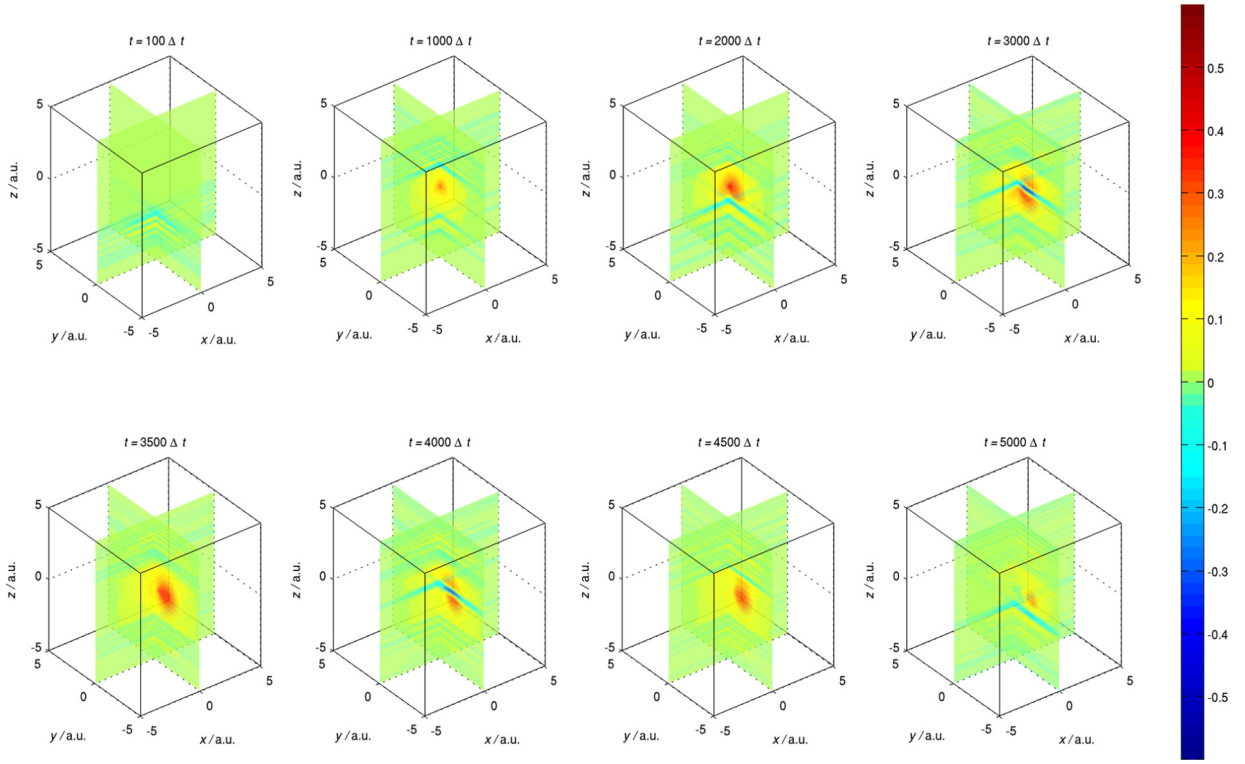

Fig. 5. Evolution of the wavefunction (imaginary part). It shows the same ionization process as in Fig. 4.

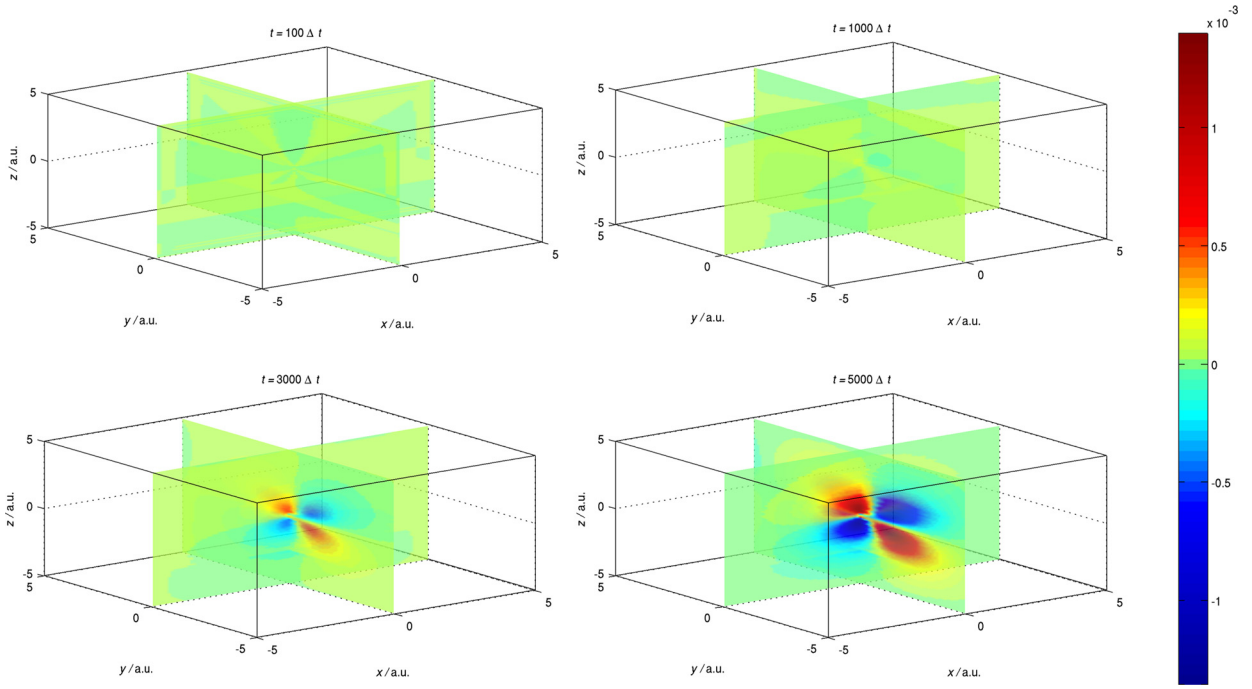

Fig. 6. Evolution of the A_z component of scattered gauge field. The scattered field dependents strongly on the electron polarization current. It is weak relative to the incident field, which indicates that the effect of a single atom is small. An ensemble with 10^3–10^4 atoms will show significant effects.

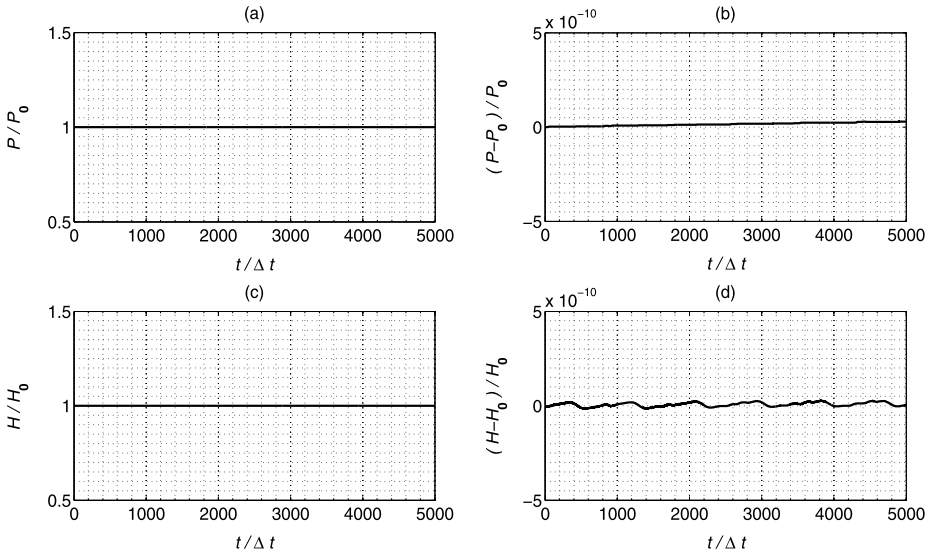

Fig. 7. Time-history of numerical errors. After a long-term simulation, both total probability error (a)–(b) and total Hamiltonian error (c)–(d) are bounded by a small value.

$\int_T \int_V \psi^*(t)\ddot{\boldsymbol{x}}\psi(t)e^{i\omega t}\mathrm{d}^3x\mathrm{d}t$ can be calculated numerically. It can also be obtained by calculating the scattered gauge field spectrum via a class of numerical probes around the potential center. Numerically calculated wave functions also contains detailed information about the dynamics of ionization. In a strong field, the atomic potential is seriously dressed, and the wave function becomes non-localized. Therefore, electrons have a chance of jumping into free states. Above a specified threshold, the stabilization will quickly appears, i.e., the ionization rate increases slowly with the growth of beam intensity and photon energy [12,14]. By introducing a proper absorbing boundary condition in the simulation, the ionization rate can be calculated as $\Gamma_I = \oint \frac{1}{2}(\psi_R \bigtriangledown \psi_I - \psi_I \bigtriangledown \psi_R)\cdot \mathrm{d}\boldsymbol{S}$, which gives a non-perturbative numerical treatment of the phenomena.

Acknowledgements

This research is supported by the National Natural Science Foundation of China (NSFC-51477182, 11575185, 11575186), ITER-China Program (2015GB111003) and Key Research Program of Frontier Sciences CAS (QYZDB-SSW-SYS004).

Appendix A. Supplementary material

Supplementary material related to this article can be found online at http://dx.doi.org/10.1016/j.jcp.2017.08.033.

References

[1] G.A. Mourou, C.L. Labaune, M. Dunne, N. Naumova, V.T. Tikhonchuk, Relativistic laser–matter interaction: from attosecond pulse generation to fast ignition, Plasma Phys. Control. Fusion 49 (2007) B667.
[2] F. Krausz, M. Ivanov, Attosecond physics, Rev. Mod. Phys. 81 (2009) 163.
[3] G. Voronov, N. Delone, Multiphoton ionization of krypton and argon by ruby laser radiation, JETP Lett. 1 (1965) 66.
[4] L.V. Keldysh, Ionization in the field of a strong electromagnetic wave, Sov. Phys. JETP 20 (1965) 1307.
[5] F.H.M. Faisal, Multiple absorption of laser photons by atoms, J. Phys. B 6 (1973) L89.
[6] P. Agostini, F. Fabre, G. Mainfray, G. Petite, N.K. Rahman, Free–free transitions following six-photon ionization of xenon atoms, Phys. Rev. Lett. 42 (1979) 1127.
[7] H.R. Reiss, Effect of an intense electromagnetic field on a weakly bound system, Phys. Rev. A 22 (1980) 1786.
[8] Y. Gontier, N.K. Rahman, M. Trahin, Multiphoton absorptions above the ionization threshold, J. Phys. B 13 (1980) 1381.
[9] A. McPherson, G. Gibson, H. Jara, U. Johann, T.S. Luk, Studies of multiphoton production of vacuum-ultraviolet radiation in the rare gases, J. Opt. Soc. Am. B 4 (1987) 595.
[10] T.F. Gallagher, Above-threshold ionization in low-frequency limit, Phys. Rev. Lett. 61 (1988) 2304.
[11] J.H. Eberly, J. Javanainen, K. Rzazewski, Above-threshold ionization, Phys. Rep. 204 (1991) 331.
[12] M. Pont, M. Gavrila, Stabilization of atom hydrogen in superintense, high-frequency laser fields of circular polarization, Phys. Rev. Lett. 65 (1990) 2362.
[13] J.L. Krause, K.J. Schafer, K.C. Kulander, High-order harmonic generation from atoms and ions in the high intensity regime, Phys. Rev. Lett. 68 (1992) 3535.
[14] J.H. Eberly, K.C. Kulander, Atomic stabilization by super-intense lasers, Science 262 (1993) 5137.
[15] P. Corkum, Plasma perspective on strong-field multiphoton ionization, Phys. Rev. Lett. 71 (1993) 1994.
[16] M. Lewenstein, P. Balcou, M. Ivanov, A. L'Huillier, P. Corkum, Theory of high-harmonic generation by low-frequency laser fields, Phys. Rev. A 49 (1994) 2117.
[17] I. Bialynicki-Birula, M. Kaliński, J.H. Eberly, Lagrange equilibrium points in celestial mechanics and nonspreading wave packets for strongly driven Rydberg electrons, Phys. Rev. Lett. 73 (1994) 1777.
[18] D. Bao, S.G. Chen, J. Liu, Rescattering effect in above-threshold ionization processes, J. Appl. Phys. B 62 (1996) 313.
[19] C. Spielmann, N.H. Burnett, S. Sartania, R. Koppitsch, M. Schnürer, C. Kan, M. Lenzner, P. Wobrauschek, F. Krausz, Generation of coherent X-rays in the water window using 5-femtosecond laser pulses, Science 278 (1997) 661.
[20] P. Salières, B. Carré, L.L. Dèroff, F. Grasbon, G.G. Paulus, H. Walther, R. Kopold, W. Becker, D.B. Milošević, A. Sanpera, M. Lewenstein, Feynman's path-integral approach for intense-laser–atom interactions, Science 292 (2001) 902.
[21] R. Kienberger, E. Goulielmakis, M. Uiberacker, A. Baltuska, V. Yakovlev, F. Bammer, A. Scrinzi, T. Westerwalbesloh, U. Kleineberg, U. Heinzmann, M. Drescher, F. Krausz, Atomic transient recorder, Nature 427 (2004) 817.
[22] R.P. Drake, High Energy Density Physics: Fundamentals, Inertial Fusion and Experimental Astrophysics, Springer, New York, 2006.
[23] T. Brabec, H. Kapteyn, Strong Field Laser Physics, Springer, New York, 2008.
[24] S. Kim, J. Jin, Y.-J. Kim, I.-Y. Park, Y. Kim, S.-W. Kim, High-harmonic generation by resonant plasmon field enhancement, Nature 453 (2008) 757.
[25] O. Smirnova, Y. Mairesse, S. Patchkovskii, N. Dudovich, D. Villeneuve, P. Corkum, M.Y. Ivanov, High harmonic interferometry of multi-electron dynamics in molecules, Nature 460 (2009) 972.
[26] A.-T. Le, R.R. Lucchese, S. Tonzani, T. Morishita, C.D. Lin, Quantitative rescattering theory for high-order harmonic generation from molecules, Phys. Rev. A 80 (2009) 013401.
[27] E. Goulielmakis, Z.-H. Loh, A. Wirth, R. Santra, N. Rohringer, V.S. Yakovlev, S. Zherebtsov, T. Pfeifer, A.M. Azzeer, M.F. Kling, S.R. Leone, F. Krausz, Real-time observation of valence electron motion, Nature 466 (2010) 739.
[28] R. Nepstad, T. Birkeland, M. Førre, Numerical study of two-photon ionization of helium using an ab initio numerical framework, Phys. Rev. A 81 (2010) 063402.
[29] T. Birkeland, R. Nepstad, M. Førre, Stabilization of helium in intense XUV laser fields, Phys. Rev. Lett. 104 (2010) 163002.
[30] T. Popmintchev, M.-C. Chen, D. Popmintchev, P. Arpin, S. Brown, S. Ališauskas, G. Andriukaitis, T. Balčiunas, O.D. Mücke, A. Pugzlys, A. Baltuška, B. Shim, S.E. Schrauth, A. Gaeta, C. Hernández-García, L. Plaja, A. Becker, A. Jaron-Becker, M.M. Murnane, H.C. Kapteyn, Bright coherent ultrahigh harmonics in the keV X-ray regime from mid-infrared femtosecond lasers, Science 336 (2012) 1287.
[31] A.D. Piazza, C. Müller, K.Z. Hatsagortsyan, C.H. Keitel, Extremely high-intensity laser interactions with fundamental quantum systems, Rev. Mod. Phys. 84 (2012) 1177.
[32] W. Becker, X. Liu, P.J. Ho, J.H. Eberly, Theories of photoelectron correlation in laser driven multiple atomic ionization, Rev. Mod. Phys. 84 (2012) 1011.
[33] C.B. Madsen, F. Anis, L.B. Madsen, B.D. Esry, Multiphoton above threshold effects in strong-field fragmentation, Phys. Rev. Lett. 109 (2012) 163003.
[34] L. Argenti, R. Pazourek, J. Feist, S. Nagele, M. Liertzer, E. Persson, J. Burgdörfer, E. Lindroth, Photoionization of helium by attosecond pulses: extraction of spectra from correlated wave functions, Phys. Rev. A 87 (2013) 053405.
[35] K.-J. Yuan, A.D. Bandrauk, Single circularly polarized attosecond pulse generation by intense few cycle elliptically polarized laser pulses and terahertz fields from molecular media, Phys. Rev. Lett. 110 (2013) 023003.
[36] L. Guo, S.S. Han, X. Liu, Y. Cheng, Z.Z. Xu, J. Fan, J. Chen, S.G. Chen, W. Becker, C.I. Blaga, A.D. DiChiara, E. Sistrunk, P. Agostini, L.F. DiMauro, Scaling of the low-energy structure in above-threshold ionization in the tunneling regime: theory and experiment, Phys. Rev. Lett. 110 (2013) 013001.
[37] M. Klaiber, E. Yakaboylu, K.Z. Hatsagortsyan, Above-threshold ionization with highly charged ions in superstrong laser fields. II. Relativistic Coulomb-corrected strong-field approximation, Phys. Rev. A 87 (2013) 023418.
[38] G. Vampa, C. McDonald, G. Orlando, D. Klug, P. Corkum, T. Brabec, Theoretical analysis of high-harmonic generation in solids, Phys. Rev. Lett. 113 (2014) 073901.
[39] S.V. Popruzhenko, Keldysh theory of strong field ionization: history, applications, difficulties and perspectives, J. Phys. B 47 (2014) 204001.

[40] D. Popmintchev, C. Hernández-García, F. Dollar, C. Mancuso, J.A. Pérez-Hernández, M.-C. Chen, A. Hankla, X. Gao, B. Shim, A.L. Gaeta, M. Tarazkar, D.A. Romanov, R.J. Levis, J.A. Gaffney, M. Foord, S.B. Libby, A. Jaron-Becker, A. Becker, L. Plaja, M.M. Murnane, H.C. Kapteyn, T. Popmintchev, Ultraviolet surprise: efficient soft X-ray high-harmonic generation in multiply ionized plasmas, Science 350 (2015) 1225.
[41] O. Kfir, P. Grychtol, E. Turgut, R. Knut, D. Zusin, D. Popmintchev, T. Popmintchev, H. Nembach, J.M. Shaw, A. Fleischer, H. Kapteyn, M. Murnane, O. Cohen, Generation of bright phase-matched circularly-polarized extreme ultraviolet high harmonics, Nat. Photonics 9 (2015) 99.
[42] T.T. Luu, M. Garg, S.Y. Kruchinin, A. Moulet, M.T. Hassan, E. Goulielmakis, Extreme ultraviolet high-harmonic spectroscopy of solids, Nature 521 (2015) 498.
[43] M. Bukov, L. D'Alessio, A. Polkovnikov, Universal high-frequency behavior of periodically driven systems: from dynamical stabilization to Floquet engineering, Adv. Phys. 64 (2015) 139.
[44] M.T. Hassan, T.T. Luu, A. Moulet, O. Raskazovskaya, P. Zhokhov, M. Garg, N. Karpowicz, A.M. Zheltikov, V. Pervak, F. Krausz, E. Goulielmakis, Optical attosecond pulses and tracking the nonlinear response of bound electrons, Nature 530 (2016) 66.
[45] P. Corkum, Recollision physics, Phys. Today 64 (2011) 36.
[46] D. Hochstuhl, C. Hinz, M. Bonitz, Time-dependent multiconfiguration methods for the numerical simulation of photoionization processes of many-electron atoms, Eur. Phys. J. Spec. Top. 223 (2014) 177.
[47] H. Miyagi, L.B. Madsen, Time-dependent restricted-active-space self-consistent-field theory for laser-driven many-electron dynamics. II. Extended formulation and numerical analysis, Phys. Rev. A 89 (2014) 063416.
[48] S. Bauch, L.K. Sørensen, L.B. Madsen, Time-dependent generalized-active-space configuration–interaction approach to photoionization dynamics of atoms and molecules, Phys. Rev. A 90 (2014) 062508.
[49] L. Wu, X. Jin, Z. Wu, Symplectic structure of Schrödinger equation and symplectic algorithms for quantum mechanics, Chin. J. Comput. Phys. 12 (1995) 127.
[50] K.S. Yee, Numerical solution of initial boundary value problems involving Maxwell's equations in isotropic media, IEEE Trans. Antennas Propag. 14 (1966) 302.
[51] G. Mur, Absorbing boundary conditions for the finite-difference approximation of the time-domain electromagnetic-field equations, IEEE Trans. Electromagn. Compat. 23 (1981) 377.
[52] J.P. Berenger, A perfectly matched layer for the absorption of electromagnetic waves, J. Comput. Phys. 114 (1994) 185.
[53] S. Blanes, F. Casas, A. Murua, Symplectic splitting operator methods for the time-dependent Schrödinger equation, J. Chem. Phys. 124 (2006) 234105.
[54] K. Kormann, S. Holmgren, H.O. Karlsson, Accurate time propagation for the Schrödinger equation with an explicitly time-dependent Hamiltonian, J. Chem. Phys. 128 (2008) 184101.
[55] J. Shen, Wei E.I. Sha, Z. Huang, M. Chen, X. Wu, High-order symplectic FDTD scheme for solving a time-dependent Schrödinger equation, Comput. Phys. Commun. 184 (2013) 445.
[56] J. Squire, H. Qin, W.M. Tang, Geometric integration of the Vlasov–Maxwell system with a variational particle-in-cell scheme, Phys. Plasmas 19 (2012) 084501.
[57] J. Xiao, J. Liu, H. Qin, Z. Yu, A variational multi-symplectic particle-in-cell algorithm with smoothing functions for the Vlasov–Maxwell system, Phys. Plasmas 20 (2013) 102517.
[58] J. Xiao, J. Liu, H. Qin, Z. Yu, N. Xiang, Variational symplectic particle-in-cell simulation of nonlinear mode conversion from extraordinary waves to Bernstein waves, Phys. Plasmas 22 (2015) 092305.
[59] J. Xiao, H. Qin, J. Liu, Y. He, R. Zhang, Y. Sun, Explicit high-order non-canonical symplectic particle-in-cell algorithms for Vlasov–Maxwell systems, Phys. Plasmas 22 (2015) 112504.
[60] Y. He, H. Qin, Y. Sun, J. Xiao, R. Zhang, J. Liu, Hamiltonian integration methods for Vlasov–Maxwell equations, Phys. Plasmas 22 (2015) 124503.
[61] H. Qin, J. Liu, J. Xiao, R. Zhang, Y. He, Y. Wang, Y. Sun, J.W. Burby, L. Ellison, Y. Zhou, Canonical symplectic particle-in-cell method for long-term large-scale simulations of the Vlasov–Maxwell equations, Nucl. Fusion 56 (2016) 014001.
[62] Y. He, Y. Sun, H. Qin, J. Liu, Hamiltonian particle-in-cell methods for Vlasov–Maxwell equations, Phys. Plasmas 23 (2016) 092108.
[63] P. Morrison, Structure and structure-preserving algorithms for plasma physics, Phys. Plasmas 24 (2017) 055502.
[64] J. Xiao, H. Qin, P. Morrison, J. Liu, Z. Yu, R. Zhang, Y. He, Explicit high-order noncanonical symplectic algorithms for ideal two-fluid systems, Phys. Plasmas 23 (2016) 112107.
[65] M. Kraus, K. Kormann, P. Morrison, E. Sonnendrücker GEMPIC, Geometric electromagnetic particle-in-cell methods, https://arxiv.org/abs/1609.03053.
[66] D. Masiello, On the Canonical Formulation of Electromagnetics and Wave Mechanics, Ph.D. thesis, University of Florida, 2004.
[67] D. Masiello, E. Deumens, Y. Öhrn, Dynamics of an atomic electron and its electromagnetic field in a cavity, Phys. Rev. A 71 (2005) 032108.
[68] L.D. Landau, E.M. Lifshitz, Quantum Mechanics: Nonrelativistic Theory, Pergamon Press, Oxford, 1965.
[69] P.A.M. Dirac, The Principles of Quantum Mechanics, 4th ed., Oxford University Press, Oxford, 1958.